Supporting Information for "FAT or FiTT: Are anvil clouds or the tropopause temperature-invariant?"

Jacob T. Seeley[1], Nadir Jeevanjee[2,3], and David M. Romps[1,4]

Contents of this file

1. Text S1 to S4
2. Figures S1 to S5

---

[1]Department of Earth and Planetary Science, University of California (Berkeley), Berkeley, CA 94720

[2]Department of Geosciences, Princeton University, Princeton, NJ 08544

[3]Geophysical Fluid Dynamics Laboratory, Princeton, NJ 08540

[4]Climate and Ecosystem Sciences Division, Lawrence Berkeley National Laboratory, Berkeley, CA 94720

Text S1: Simulations All simulations were conducted with DAM (Romps, 2008), a three-dimensional, fully compressible, nonhydrostatic CRM that computes radiative transfer with RRTM (Clough et al., 2005; Iacono et al., 2008). The simulations used a square domain with a side length of 48 km and doubly periodic horizontal boundaries. The horizontal resolution was 500 m, and the vertical grid spacing increased from 50 m in the boundary layer to a constant 250 m spacing for altitudes between 3 km and 30 km, and increased again to a spacing of 1 km between 40 km and the model top at 50 km. Surface fluxes were computed via a standard bulk aerodynamic formula. Horizontal-mean winds were damped to zero on a time scale of six hours, and wave damping was applied to the 3-dimensional stratospheric wind field.

In the "minimal-recipe" simulations, longwave emission from water vapor is the only contributor to radiative heating rates. This is accomplished by turning off shortwave radiation and zeroing out carbon dioxide, ozone, and condensed water in the radiative transfer calculations. In addition, the minimal-recipe simulations use a simplified autoconversion-based microphysics scheme that has been described in previous work (Seeley, Jeevanjee, Langhans, & Romps, 2019). Other than the condensation and evaporation that occur during saturation adjustment, the only microphysical process included in this scheme is autoconversion of cloud condensate to rain, which is given a fixed e-folding timescale of 30 minutes. Rain is given a fixed freefall speed of 10 m/s and is allowed to evaporate in subsaturated air. In comparison, the "full-complexity" simulations include shortwave radiation, a vertically-uniform 280 ppmv of carbon dioxide, interactive cloud radiation, and use DAM's default Lin-Lord-Krueger microphysics scheme (Krueger, Fu, Liou, &

Chin, 1995; Lin, Farley, & Orville, 1983; Lord, Willoughby, & Piotrowicz, 1984). The rain-evaporation parameterization used in the minimal-recipe simulations is that of the Lin-Lord-Krueger scheme.

For each of the two model configurations, six simulations were run over fixed sea surface temperatures T_s ranging from 260 to 310 K, for a total of twelve simulations. Each simulation was initialized with thermodynamic profiles generated by analytical solutions to RCE, and run to equilibrium over 1000 days with a coarser horizontal resolution (2 km). The simulations were then restarted with 500 m horizontal resolution and run to equilibrium, with the last 50 days of the simulations being averaged for statistics. Cloudy grid points were identified as those with cloud condensate mass fraction larger than 10^{-5} kg/kg.

Text S2: Calculating detrainment We calculate detrainment using the bulk-plume budget for a tracer that is conserved in cloudy air. This tracer is the "purity" tracer, ϕ (kg/kg), which is set to 1 below cloud base and to 0 in clear air that is some distance away from cloudy air in the free troposphere at every time step (Romps & Kuang, 2010a, 2010b). The steady-state budget for the value of this tracer in the convective plume, ϕ_c, is

$$\partial_z \phi_c = -\varepsilon \phi_c, \tag{1}$$

where $\varepsilon = E/M_c$ (m^{-1}) is the fractional entrainment rate. In (1), we have made the approximation that the mixing ratio of the purity tracer in environmental air, ϕ_e, is 0; this is guaranteed to be very nearly true by the zeroing-out of purity in non-cloudy air at every time step. We record ϕ_c as part of the statistics collected over the last 50

days of the RCE simulations, which allows us to quantify the steady-state entrainment rate: $E = \varepsilon M_c = -M_c \partial_z \phi_c / \phi_c$. Using the equation for mass continuity of the plume ($\partial_z M_c = E - D$), we can then solve for the detrainment rate:

$$D = -M_c \partial_z \phi_c / \phi_c - \partial_z M_c. \tag{2}$$

The profiles of detrainment obtained by this method are plotted in Figure 2c of the main text.

Text S3: Longwave radiative cooling from water vapor

This section focuses on the longwave radiative cooling from water vapor. One piece of the theoretical support for the FAT hypothesis is the idea that the longwave radiative cooling from water vapor should decline rapidly at a particular temperature — a temperature that is reached in the upper troposphere of Earth's current tropics (Eitzen, Xu, & Wong, 2009; Harrop & Hartmann, 2012; D. Hartmann & Larson, 2002; Kuang & Hartmann, 2007; Kubar, Hartmann, & Wood, 2007; Larson & Hartmann, 2003; Li, Yang, North, & Dessler, 2012; Thompson, Bony, & Li, 2017; Xu et al., 2007; Zelinka & Hartmann, 2010, 2011). This claim is based on the idea that longwave emissivity controls the amplitude of radiative cooling, and that radiative cooling must therefore decline rapidly with the exponentially-falling upper-tropospheric water-vapor concentrations.

This claim appears to be true if water vapor is assumed to be a gray gas (i.e., assumed to have an absorption coefficient that is independent of wavenumber). In Figure S1, we compare the longwave radiative cooling rates from our minimal-recipe RCE simulations as computed by a gray radiation scheme and by RRTM (Clough et al., 2005; Iacono et al., 2008). We arbitrarily set the absorption coefficient κ of the gray scheme to 15 kg/m^2.

(Changing this value changes the temperature at which radiative cooling peaks, but not the qualitative behavior.) In the gray scenario (Fig. S1a,b), radiative cooling is narrowly peaked around the altitude where the longwave optical depth (τ) equals 1 (Pierrehumbert, 2010). This level occurs at an approximately fixed temperature because water vapor density in RCE is a nearly invariant function of temperature. As a result, radiative cooling in this scenario declines with height most rapidly at an approximately fixed temperature (roughly 225 K) that occurs on the cold side of the $\tau = 1$ level. Therefore, Statement 5 from the main text ("Clear-sky radiative cooling must decline most rapidly with height at a fixed temperature") would appear to be true if water vapor were a gray gas.

Of course, it is well-known that water vapor is not a gray gas. What are the implications of this non-gray physics for the shape of the radiative cooling profile? When radiative transfer is computed by RRTM (Fig. S1c,d), the longwave cooling from water vapor is spread out smoothly over the depth of the troposphere rather than being sharply peaked at one particular level. The longwave cooling computed by RRTM still collapses onto an approximately universal curve in temperature coordinates, as has been previously demonstrated and explained theoretically (Jeevanjee & Romps, 2018). But, this invariant curve declines smoothly as a function of temperature in the bulk of the troposphere, with no especially rapid decline at any particular temperature.

The simplicity of this collapse of radiative cooling profiles is lost for other ways of plotting the cooling rate. For example, when the cooling rate is expressed as a temperature tendency (i.e., in units of K/day), one gets the impression that radiative cooling changes in a complex way as a function of surface temperature (Fig. S2). This is true whether the

cooling rate is plotted with temperature, pressure, or altitude as the vertical coordinate (Fig. S2a,b,c, respectively).

Under what conditions, or in what sense, is there a rapid decline in radiative cooling at the top of the troposphere? The apparent sharpness of the top of the water-vapor cooling profile can be found in the literature going back decades (e.g., Clough, Iacono, & Moncet, 1992; D. L. Hartmann, Holton, & Fu, 2001; Manabe & Strickler, 1964). These results show radiative temperature tendencies (in K/day) as a function of pressure taking on an approximately fixed value throughout most of the troposphere and then dropping to zero over the course of 100 mb or so. However, our results indicate that such a shape depends on a particular choice of coordinates and only exists over a certain range of surface temperatures. In Figure 3a of the main text, we show that radiative heating rates in W/m^3 (i.e., as flux divergences) decline smoothly over the depth of the troposphere, with no particularly rapid decline or kink at any particular temperature. If we convert to the unit of K/day and use pressure as a vertical coordinate (figure S2b), we do reproduce the kinked shape for surface temperatures of 300 K or warmer, but for colder surface temperatures, the kink disappears.

To check that the disappearance of the kink is not an artifact of approximations in the RRTM radiative transfer scheme, we recalculated cooling rates with the line-by-line code RFM (Dudhia, 2017). The line-by-line calculations use a spectral resolution of 0.25 cm^{-1} and the results are integrated over the wavenumber range 0.25–3000 cm^{-1} to yield total fluxes and cooling rates, and the two-stream approximation is used with a diffusivity factor of 1.5 to account for hemispheric integration. The results of the RFM calculations

match the RRTM cooling profiles quite well, and reproduce the disappearance of the kink in radiative cooling at cooler surface temperatures.

Therefore, we can conclude that the ubiquity of the kinked shape of water-vapor cooling profiles in the literature derives from (a) the conventional choice of plotting coordinates, and (b) the exploration of a relatively small range of surface temperatures. However, since extensive anvil clouds persist in all of our simulations, it seems erroneous to attribute them to a particular kinked shape of radiative cooling that only exists at surface temperatures similar to Earth's current tropics.

Text S4: Decomposition of clear-sky convergence This section uses equation 2 of the main text to diagnose the source of the upper-tropospheric clear-sky convergence peaks in our simulations. Using the fact that the clear-sky diabatic cooling rate Q_e is the sum of radiative (R_e) and latent (L_e) cooling terms, the approximate expression for clear-sky convergence (the RHS of equation 2 in the main text) can be decomposed into 4 terms:

$$\frac{\partial M_e}{\partial z} = \underbrace{-\frac{1}{c_p\left(\Gamma_d-\Gamma\right)}\frac{\partial R_e}{\partial z}}_{\text{term 1}} \underbrace{-\frac{1}{c_p\left(\Gamma_d-\Gamma\right)}\frac{\partial L_e}{\partial z}}_{\text{term 2}} \underbrace{-\frac{R_e}{c_p\left(\Gamma_d-\Gamma\right)^2}\frac{\partial \Gamma}{\partial z}}_{\text{term 3}} \underbrace{-\frac{L_e}{c_p\left(\Gamma_d-\Gamma\right)^2}\frac{\partial \Gamma}{\partial z}}_{\text{term 4}} \quad (3)$$

These four terms and their sum are plotted alongside the actual clear-sky convergence from each of the six minimal-recipe simulations in Figure 3. The sum of the terms is a reasonable approximation to the actual clear-sky convergence in all simulations. Generally, there is a rough cancellation between terms 2 and 4, which involve the profile of latent cooling. The upper-tropospheric peak in clear-sky convergence tends to be co-located with a peak in

term 1. This clear-sky convergence peak is accentuated by term 3, which is negative and peaks in the mid-troposphere, thereby carving out the positive mid-tropospheric values of term 1 and leaving in relief a sharper peak for their sum. Nevertheless, this general behavior suggests that the upper-tropospheric peak in clear-sky convergence can be mainly attributed to term 1.

Turning to term 1, then, the question becomes: why does this term peak in the upper troposphere? Since $[c_p(\Gamma_d - \Gamma)]^{-1}$ and $-\partial R_e/\partial z$ both vary with height, we must look at the profiles of these two quantities to see which peaks in the upper troposphere. Figures 4–5 plot these two quantities for the minimal-recipe simulations. Those figures demonstrate that upper-tropospheric peak in term 1 is caused by the peak in $[c_p(\Gamma_d - \Gamma)]^{-1}$, not $-\partial R_e/\partial z$. Therefore, this analysis implies that the clear-sky convergence peak near the anvil level is primarily caused by the minimum in static stability there, not by an especially rapid decline in radiative cooling below the tropopause.

References

Clough, S. A., Iacono, M. J., & Moncet, J.-l. (1992). Line-by-line calculations of atmospheric fluxes and cooling rates: application to water vapor. *Journal of Geophysical Research*, *97*.

Clough, S. A., Shephard, M. W., Mlawer, E. J., Delamere, J. S., Iacono, M. J., Cady-Pereira, K., ... Brown, P. D. (2005). Atmospheric radiative transfer modeling: A summary of the AER codes. *Journal of Quantitative Spectroscopy and Radiative Transfer*, *91*(2), 233–244. doi: 10.1016/j.jqsrt.2004.05.058

Dudhia, A. (2017). Journal of Quantitative Spectroscopy & Radia-

tive Transfer The Reference Forward Model (RFM). *Journal of Quantitative Spectroscopy and Radiative Transfer*, *186*, 243–253. Retrieved from http://dx.doi.org/10.1016/j.jqsrt.2016.06.018 doi: 10.1016/j.jqsrt.2016.06.018

Eitzen, Z. A., Xu, K. M., & Wong, T. (2009). Cloud and radiative characteristics of tropical deep convective systems in extended cloud objects from CERES observations. *Journal of Climate*, *22*(22), 5983–6000. doi: 10.1175/2009JCLI3038.1

Harrop, B. E., & Hartmann, D. L. (2012). Testing the Role of Radiation in Determining Tropical Cloud-Top Temperature. *Journal of Climate*, *25*(2007), 5731–5747. doi: 10.1175/JCLI-D-11-00445.1

Hartmann, D., & Larson, K. (2002). An important constraint on tropical cloudclimate feedback. *Geophysical Research Letters*, *29*(20), 10–13. doi: 10.1029/2002GL015835

Hartmann, D. L., Holton, J. R., & Fu, Q. (2001). The heat balance of the tropical tropopause, cirrus, and stratospheric dehydration. *Geophysical Research Letters*, *28*(10), 1969–1972.

Iacono, M. J., Delamere, J. S., Mlawer, E. J., Shephard, M. W., Clough, S. A., & Collins, W. D. (2008). Radiative forcing by long-lived greenhouse gases: Calculations with the AER radiative transfer models. *Journal of Geophysical Research Atmospheres*, *113*(13), 2–9. doi: 10.1029/2008JD009944

Jeevanjee, N., & Romps, D. (2018). Mean Precipitation Change from a Deepening Troposphere. *Proceedings of the National Academy of Sciences*, *in press*, 1–12. Retrieved from https://arxiv.org/abs/1711.03516

Krueger, S. K., Fu, Q., Liou, K. N., & Chin, H.-N. S. (1995). Improvements of an ice-phase mcrophysics parameterization for use in numerical simulations of tropical convection. *Journal of Applied Meteorology*, *34*(1).

Kuang, Z., & Hartmann, D. L. (2007, may). Testing the Fixed Anvil Temperature Hypothesis in a Cloud-Resolving Model. *Journal of Climate*, *20*(10), 2051–2057. doi: 10.1175/JCLI4124.1

Kubar, T., Hartmann, D. L., & Wood, R. (2007). Radiative and Convective Driving of Tropical High Clouds. *Journal of Climate*, *20*, 5510–5527. doi: 10.1175/2007JCLI1628.1

Larson, K., & Hartmann, D. L. (2003). Interactions among Cloud , Water Vapor , Radiation , and Large-Scale Circulation in the Tropical Climate . Part I : Sensitivity to Uniform Sea Surface Temperature Changes. *Journal of Climate*, 1425–1440.

Li, Y., Yang, P., North, G. R., & Dessler, A. (2012). Test of the Fixed Anvil Temperature Hypothesis. *Journal of the Atmospheric Sciences*, *69*. doi: 10.1175/JAS-D-11-0158.1

Lin, Y.-L., Farley, R. D., & Orville, H. D. (1983). Bulk parameterization of the snow field in a cloud model. *Journal of Climate and Applied Meteorology*, *22*.

Lord, S. J., Willoughby, H. E., & Piotrowicz, J. M. (1984). *Role of a Parameterized Ice-Phase Microphysics in an Axisymmetric, Nonhydrostatic Tropical Cyclone Model* (Vol. 41). doi: 10.1175/1520-0469(1984)041¡2836:ROAPIP¿2.0.CO;2

Manabe, S., & Strickler, R. F. (1964). Thermal equilibrium of the atmosphere with a convective adjustment. *Journal of the Atmospheric Sciences*, *21*.

Pierrehumbert, R. T. (2010). *Principles of Planetary Climate*. Cambridge University Press.

Romps, D. M. (2008, dec). The Dry-Entropy Budget of a Moist Atmosphere. *Journal of the Atmospheric Sciences*, *65*(12), 3779–3799. doi: 10.1175/2008JAS2679.1

Romps, D. M., & Kuang, Z. (2010a, feb). Do Undiluted Convective Plumes Exist in the Upper Tropical Troposphere? *Journal of the Atmospheric Sciences*, *67*(2), 468–484. doi: 10.1175/2009JAS3184.1

Romps, D. M., & Kuang, Z. (2010b, may). Nature versus Nurture in Shallow Convection. *Journal of the Atmospheric Sciences*, *67*(5), 1655–1666. doi: 10.1175/2009JAS3307.1

Seeley, J. T., Jeevanjee, N., Langhans, W., & Romps, D. M. (2019). Formation of tropical anvil clouds by slow evaporation. *Geophysical Research Letters*, *46*.

Thompson, D. W. J., Bony, S., & Li, Y. (2017). Thermodynamic constraint on the depth of the global tropospheric circulation. *Proceedings of the National Academy of Sciences*. doi: 10.1073/pnas.1620493114

Xu, K.-M., Wong, T., Wielicki, B., Parker, L., Lin, B., Eitzen, Z., & Branson, M. (2007). Statistical Analyses of Satellite Cloud Object Data from CERES . Part II : Tropical Convective Cloud Objects during 1998 El Niño and Evidence for Supporting. *Journal of Climate*, 819–842. doi: 10.1175/JCLI4069.1

Zelinka, M. D., & Hartmann, D. L. (2010). Why is longwave cloud feedback positive ? *Journal of Geophysical Research*, *115*(March), 1–16. doi: 10.1029/2010JD013817

Zelinka, M. D., & Hartmann, D. L. (2011). The observed sensitivity of high clouds to

mean surface temperature anomalies in the tropics. *Journal of Geophysical Research: Atmospheres*, *116*(23), 1–16. doi: 10.1029/2011JD016459

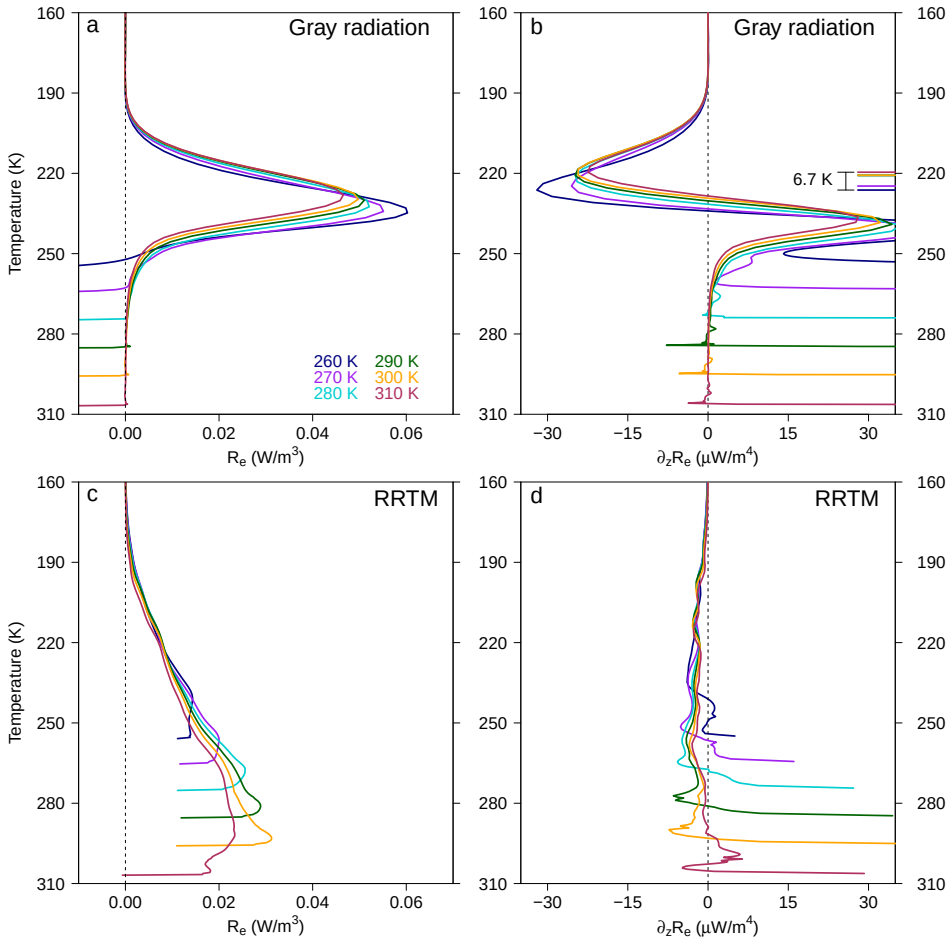

Figure 1. (a) Clear-sky longwave radiative cooling rates R_e (W/m^3, positive values for cooling) from the minimal-recipe RCE simulations as computed by a gray radiation scheme. (b) The rate of decline with height of the clear-sky longwave radiative cooling rate, $\partial_z R_e$, also from the gray scheme. (c,d) As in (a,b), but with radiative transfer computed by RRTM instead of the gray scheme. The surface temperature of each simulation is indicated by line color. In (b), the colored horizontal lines mark the temperatures at which radiative cooling declines most rapidly with height.

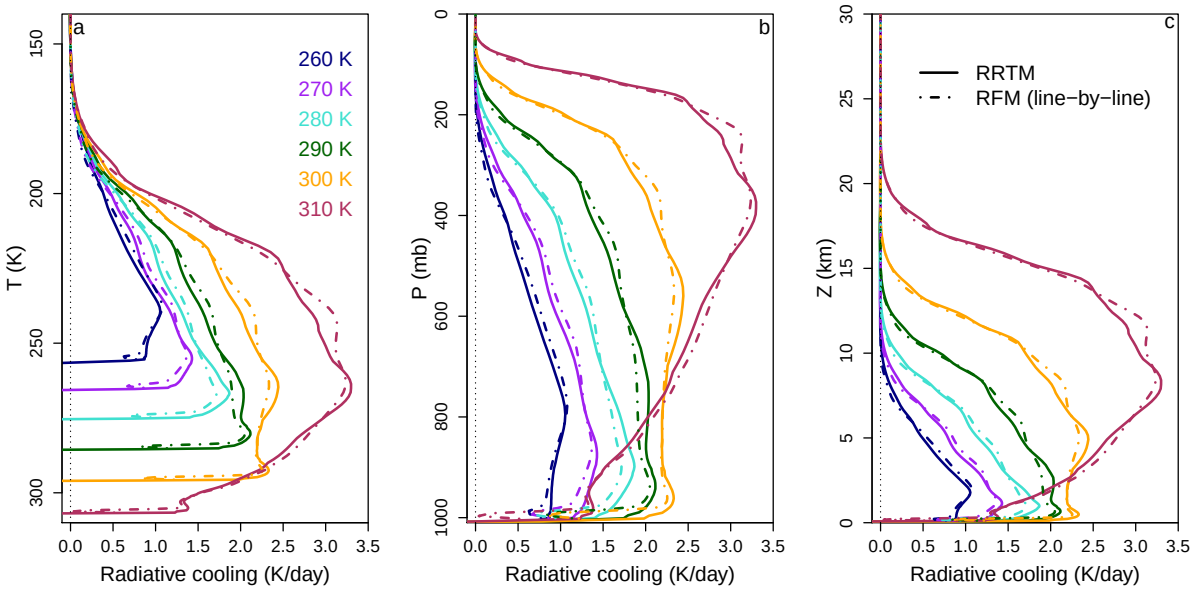

Figure 2. Clear-sky longwave radiative cooling from the minimal-recipe RCE simulations, expressed as a temperature tendency (K/day) and plotted as a function of (a) temperature, (b) pressure, and (c) altitude. The surface temperature of each simulation is indicated by line color. RRTM results are shown in solid lines, while RFM results are shown in dot-dashed lines.

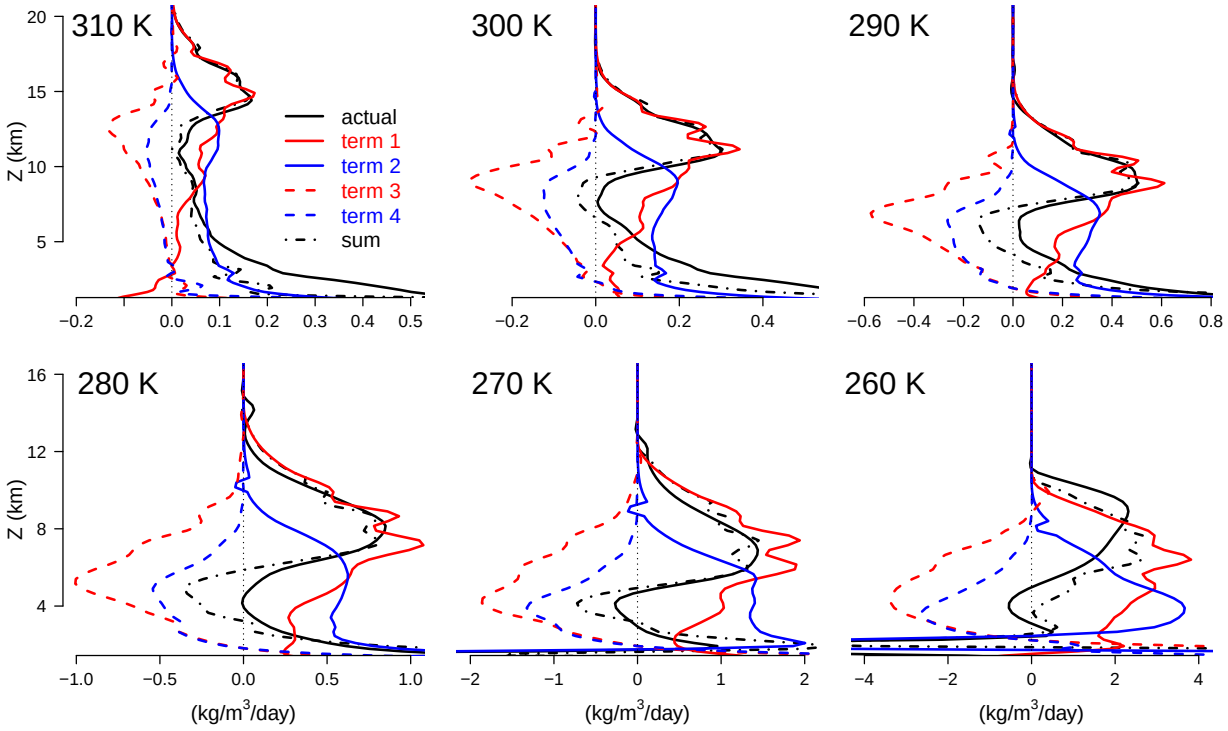

Figure 3. For the minimal-recipe simulations, an approximate decomposition of the clear-sky convergence into contributions from various terms given in equation 3.

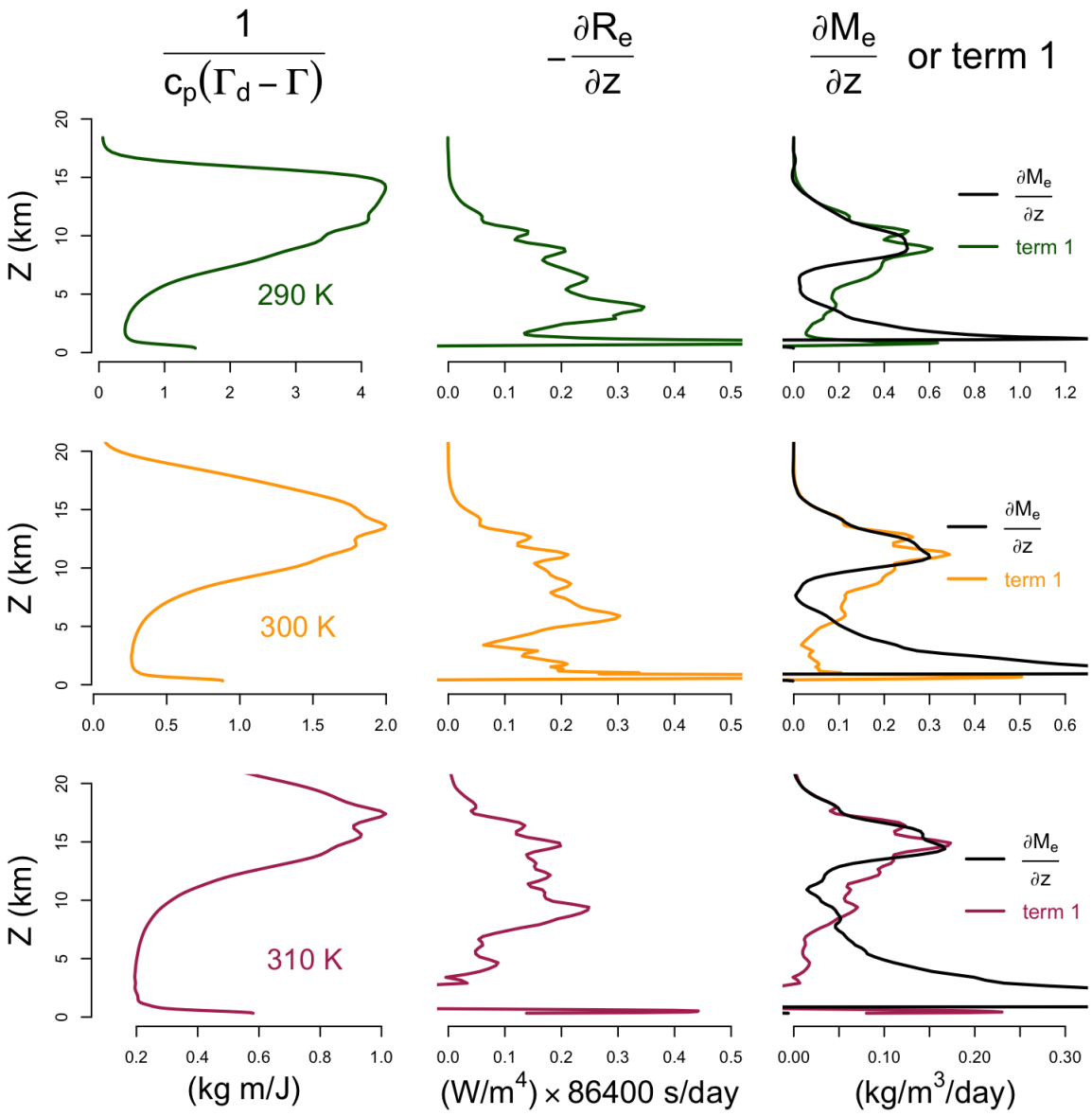

Figure 4. Further diagnosis of the origin of the upper-tropospheric clear-sky convergence peak in the minimal-recipe simulations with surface temperatures of 290 K (top row), 300 K (middle row), and 310 K (bottom row). The first two columns decompose term 1 from the RHS of equation 3 into $[c_p(\Gamma_d - \Gamma)]^{-1}$ and $-\partial R_e/\partial z$. The third column shows the product of the first two columns (i.e., term 1) in comparison to the clear-sky convergence, $\partial M_e/\partial z$.

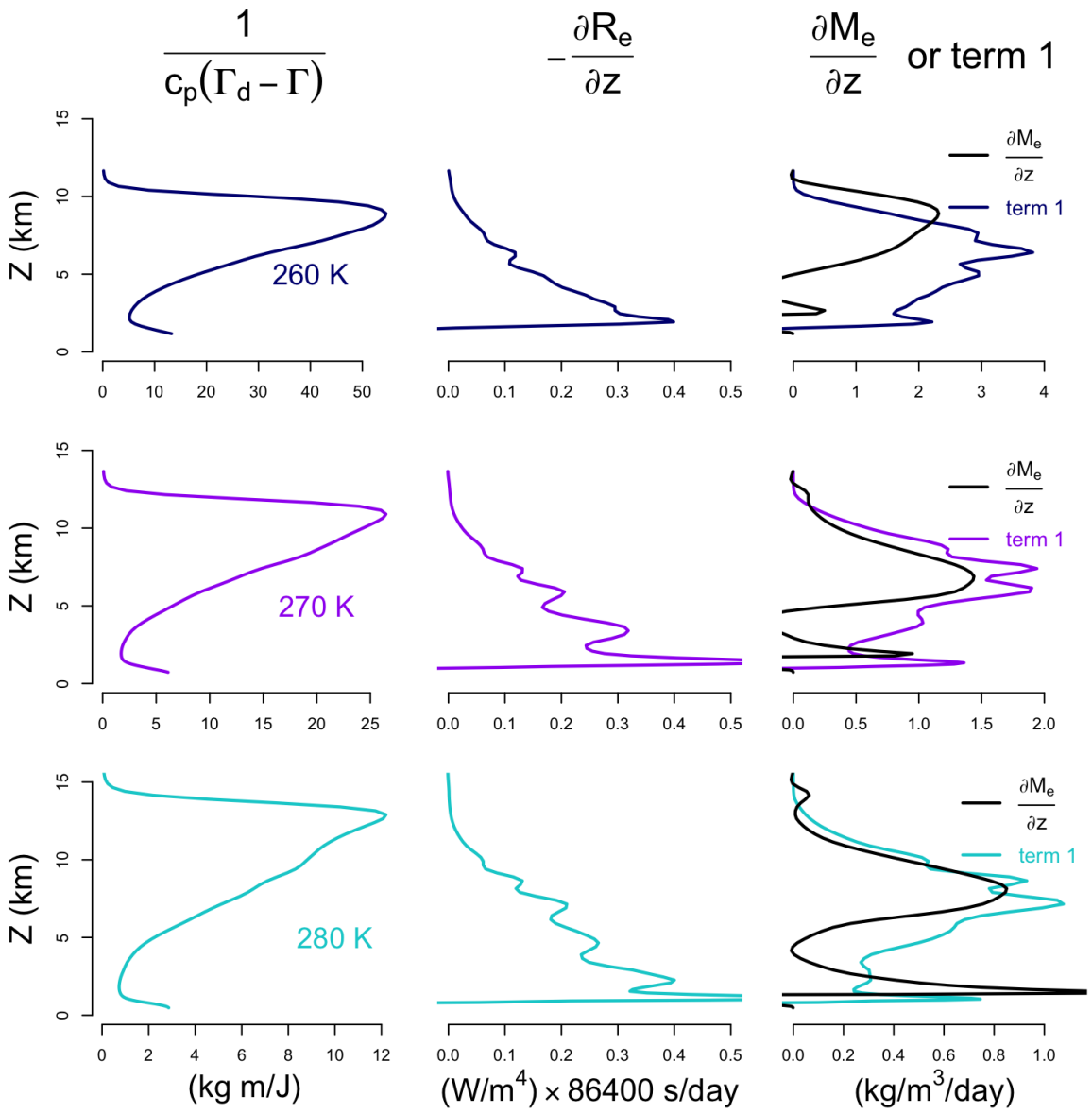

Figure 5. As in Figure 4, but for the simulations with surface temperatures of 260 K (top row), 270 K (middle row), and 280 K (bottom row).